

# A Peroxidase-like Single-Atom Fe-N5 Active Site for Effective Killing Human Lung Adenocarcinoma Cells

**Liye Zhu**

China Agricultural University

**Hong Zhong**

Washington State University

**Dan Du**

Washington State University

**Tao Li**

Northern Illinois University

**Hoai Nguyen**

Argonne National Laboratory

**Scott P. Beckman**

Washington State University

**Wentao Xu**

China Agricultural University

**Jin-Cheng Li**

Kunming University of Science and Technology

**Nan Cheng** (✉ [Goodluckchengnan@163.com](mailto:Goodluckchengnan@163.com))

China Agricultural University

**Yuehe Lin**

Washington State University

---

## Research article

**Keywords:** single-atom catalyst, 3D cancer cell model, peroxidase-like catalytic activity, cancer therapy

**Posted Date:** May 25th, 2022

**DOI:** <https://doi.org/10.21203/rs.3.rs-1629869/v1>

**License:** © ⓘ This work is licensed under a Creative Commons Attribution 4.0 International License.

[Read Full License](#)

---

# Abstract

## Background

Single-atom catalyst (SAC) is one of the newest catalysts, and attracting people's wide attention in cancer therapy based on their characteristics of maximum specific catalytic activity and high stability.

## Methods

This study designed and synthesized a Fe-N decorated graphene nanosheet (Fe-N<sub>5</sub>/GN SAC) with the coordination number of five. Its material characteristics were detected by different methods including scanning electron microscopy, transmission electron microscopy, and X-ray photoelectron spectroscopy. Also, its enzyme-like properties were calculated based on Density functional theory (DFT). In addition, 3D cancer cell models were constructed and cytotoxic effects of Fe-N<sub>5</sub>/GN SAC were tested by flow cytometry and RT-PCR.

## Results

Through enzymology and theoretical calculations, the Fe-N<sub>5</sub>/GN SAC has outstanding intrinsic peroxidase-like catalytic activity due to single-atom Fe site with five-N-coordination structure. It could kill human lung adenocarcinoma cells (A549) by decomposing hydrogen peroxide (H<sub>2</sub>O<sub>2</sub>) into toxic ROS under acidic microenvironment condition to induce the cell apoptosis in 3D lung cancer cell model.

## Conclusion

Our study synthesized a novel SAC with peroxidase-like catalytic activity for tumor therapy. And it demonstrates a promising application of SAC with highly efficient single-atom catalytic sites for cancer treatment.

## Introduction

Lung cancer is one of the most common occurrence and fatality cancer in worldwide. There are 2.2 million new cases and 1.75 million deaths per year [1]. As the improvement of understanding of lung cancer biology, the diagnose and therapy projects of lung cancer have a remarkable development. In addition to conventional chemotherapy, new therapeutic opportunities including targeted therapy and immunotherapy catch people's attention. Furthermore, more and more therapy strategies were designed based on the unique tumor microenvironment (TME). As we known, the TME is hypoxia, mildly acidic, and overproducing H<sub>2</sub>O<sub>2</sub> (5-10x10<sup>-5</sup> M) [2]. These characteristics have been applied in some new treatment strategies on cancers, especially in nano-catalytic therapy.

In recent years, nano-catalysts has been researched in biomedical field including biosensing [3, 4], antibacterial [5], and biomedicine [6–8]. All of these applications were because of nano-catalysts' unique properties of peroxidase-, oxidase-, superoxide dismutase-, and catalase-like activities. In biomedicine field, these researches focused on some cancer therapy, including pancreatic cancer [2], esophageal cancer [9], breast cancer [10], and malignant glioma [11]. Although these nano-catalysts have been used widely, their weakness are still apparent: 1) an inhomogeneous elemental composition of nanomaterials; 2) poor catalytic specificity; 3) complex catalytic mechanisms [12]. These drawbacks limited their catalytic capacity and catalytic selectivity. Moreover, they limited the development and biomedical applications of nano-catalysts. To overcome these drawbacks, developing new nano-catalysts which mimic the active sites and spatial configuration of natural enzymes [12] is the key.

Single-atom catalysts (SACs), a new type of nano-catalysts, have great promise in the applications because of higher catalytic activity compared to common nano-catalysts [12]. SACs characterized by atomically dispersed active sites, designable geometric structure, and electronic coordination, provide great opportunities to mimic the structure of natural peroxidase and thus exhibit superior catalytic performance. Therefore, SACs are one of the most potential candidates for replacing natural enzymes. In particular, Zhao and co-workers found that Fe-N<sub>4</sub> decorated zeolitic-imidazolate-framework (ZIF-8) exhibited excellent peroxidase-like property, exceeding those of Fe<sub>3</sub>O<sub>4</sub> nano-catalysts by a factor of 40 [13, 14]. Xu and co-workers have shown that atomic Zn-N<sub>4</sub> decorated ZIF-8 derivative can serve as a highly efficient peroxidase mimic for wound antibacterial applications [15]. In previous study from our team, we used atomic Fe-N<sub>4</sub> decorated carbon nanotube or ZIF-8 as the signaling element in a series of paper-based bioassays for ultrasensitive detection of H<sub>2</sub>O<sub>2</sub>, glucose, ascorbic acid, and pesticides [16–18]. By controlling the morphology and structure of SACs, high peroxidase-like activity can be achieved. It shows the great potential for lung cancer therapy.

For imitating TME in vivo model, we established a 3D lung cancer cell model in this study. It is closer to the complex in vivo conditions, and could not only eliminate the differences of cell line and animal models, but also overcome the shortcomings of individual differences in animal experiments. Moreover, the 3D cancer cell model could reserve key characteristics of in vivo models, such as cell genotypes and TME [13, 19]. These models are emerging and applying in biomedical fields including drug screening, tumor therapy, and toxicology evaluation [13, 20]. It is gradually replacing 2D cancer cell model. Therefore, we introduced 3D cancer cell model in this study to explore potential application of new SAC in lung cancer therapy.

Herein, we synthesized a novel SAC with peroxidase-like catalytic activity for tumor therapy (Scheme 1). Specifically, Fe-N decorated graphene nanosheet (Fe-N<sub>5</sub>/GN SAC), featured single-atom Fe site with five-N-coordination structure, was careful designed and synthesized as a representative SAC. This Fe-N<sub>5</sub>/GN SACbeliver was employed as a natural enzyme mimic and showed superior peroxidase-like activity. Density functional theory (DFT) calculations revealed that the reaction process to generate hydroxyl radicals is via catalytic H<sub>2</sub>O<sub>2</sub> decomposition. Finally, the SAC was used in a 3D cancer cell model to kill

lung cancer cells by inducing the excess toxic ROS and apoptosis to demonstrate the great potential of the SAC in tumor therapy. We believe this work will provide a promising application of SAC with highly efficient single-atom catalytic sites for cancer treatment.

## Materials And Methods

### Materials

Human lung adenocarcinoma cell line (A549) was purchased from National Biomedical Experimental Cell Resource (BMCR) (China). Dulbecco's minimal essential medium (DMEM), 100x Penicillin-Streptomycin-Amphotericin B, 0.25% trypsin (w/v) containing 0.52 mM EDTA were purchased from Gibco company (USA). And fetal bovine serum (FBS) was from HyClone company (USA). All the chemicals were of analytical grade. Unless otherwise stated, all solutions were prepared with ultrapure water from Barnstead Nanopure Water System.

### Preparation of Fe-N<sub>5</sub> decorated graphene nanosheet (Fe-N<sub>5</sub>/GN SAC)

Firstly, 50 mg of graphene oxide was dispersed in 60 ml 0.2 M HCl solution and mixed with 0.5 ml pyrrole, followed by 30 min sonication and 3 h vigorous stirring. Subsequently, 1.0 g ammonium peroxydisulfate (APS) was added dropwise to the above mixture under continuous stirring at room temperature. After stirring for 24 h to allow polymerization, the product was separated by vacuum filtration and washed with ethanol and water. The wet hybrid was then dispersed in 100 ml mixture solution of potassium chloride (2.98 g) and potassium ferricyanide (0.658 g), followed by 5 min sonication and 24 h vigorous stirring. This hybrid precursor was collected by vacuum filtration and dried at 60°C for 12 h and pyrolyzed at 900°C under N<sub>2</sub> atmosphere for 30 min and NH<sub>3</sub> atmosphere for 30 min. The obtained carbon material was soaked in with a 0.5 M H<sub>2</sub>SO<sub>4</sub> solution at 60°C for 4 h to remove KCl and unstable Fe species and then annealed at 900°C under NH<sub>3</sub> atmosphere for 30 min to achieve atomically dispersed Fe-N-doped graphene (Fe-N<sub>5</sub>/GN SAC).

### Material characterization

The material was characterized using scanning electron microscopy (SEM, FEI Sirion 200, operated at 30 kV), transmission electron microscopy (TEM, Tecnai G2 T20, 200 kV; Titan G 60-300 S/TEM, 60 kV, FEI, Hillsboro), and X-ray photoelectron spectroscopy (XPS, Escalab 250, Al K $\alpha$ ). The X-ray absorption spectroscopy measurement at Fe K-edge was performed at the Advanced Photon Source (APS) on the bending-magnet beamline 12-BM and 20-BM with electron energy of 7 GeV and average current of 100 mA. The radiation was monochromatized by a Si (111) double-crystal monochromator. Harmonic rejection was accomplished with Harmonic rejection mirror. All spectra were collected in fluorescence mode by vortex four-element silicon drift detector. XAS data reduction and analysis were processed by Athena software.

### Evaluation of enzyme-like properties

Enzyme-like properties were evaluated following the previous method [21]. To verify the peroxidase-like feature, 10  $\mu\text{L}$  of 0.8 mM TMB solution and 1  $\mu\text{L}$  of 1 M  $\text{H}_2\text{O}_2$  solution were first added to 0.488 mL of 0.2 M NaAc-HAc buffer (pH 3.5), and then 1  $\mu\text{L}$  of 0.05 mg/mL Fe-N<sub>5</sub>/GN SAC solution was added to the above mixture. To evaluate the catalytic activity units (U) of Fe-N<sub>5</sub>/SAC, the absorbance at 652 nm was immediately recorded at a 15 s interval within 1200 s. After subtracting the background, the catalyst activity expressed in units (U) was calculated according to the following equation:

$$b_{\text{catalyst}} = \frac{V}{\epsilon l} \times \frac{\Delta A}{\Delta t}$$

where  $b_{\text{catalyst}}$  is the catalyst activity (U),  $V$  is the volume of reaction solution ( $\mu\text{L}$ ),  $\epsilon$  is the molar absorption coefficient of the TMB substrate ( $39,000 \text{ M}^{-1} \text{ cm}^{-1}$  at 652 nm),  $l$  is the optical path length through reaction solution (cm), and  $\Delta A/\Delta t$  is the initial rate (within 1 min) of the absorbance change ( $\text{min}^{-1}$ ). When using different amounts of Fe-N<sub>5</sub>/GN SAC to measure the peroxidase-like activity, the specific activity of catalyst was determined using the following equation:

$$a_{\text{catalyst}} = \frac{b_{\text{catalyst}}}{m}$$

where  $a_{\text{catalyst}}$  is the specific activity of catalyst ( $\text{U mg}^{-1}$ ), and  $m$  is the catalyst amount (mg).

For the steady-state kinetic measurements of peroxidase-like Fe-N<sub>5</sub>/GN SAC, 10  $\mu\text{L}$  of various concentrations of TMB solution (from 0 to 3.5 mM) and 1  $\mu\text{L}$  of 1 M  $\text{H}_2\text{O}_2$  solution were added to NaAc-HAc buffer (pH 4.0). After 1  $\mu\text{L}$  of 0.05 mg/mL Fe-N<sub>5</sub>/GN SAC solution was added and mixed together for reaction, the absorbance at 652 nm was immediately recorded at a 10 s interval within 60 s. Then, the initial rates of the chromogenic reaction upon different concentrations TMB were obtained. The substrate concentration-dependent reaction rate curves were fitted with the Michaelis-Menten model. The maximum reaction rate  $v_{\text{max}}$  and Michaelis constant  $K_{\text{m}}$  were calculated according the following Michaelis-Menten equation:

$$v = \frac{v_{\text{max}}[S]}{K_{\text{m}} + [S]}$$

where  $v$  is the initial rate of the chromogenic reaction, and  $[S]$  is the TMB concentration. The catalytic constant  $k_{\text{cat}}$  was calculated using the following equation:

$$k_{\text{cat}} = \frac{v_{\text{max}}}{[E]}$$

where  $[E]$  is the catalyst concentration (M).

## Density functional theory (DFT) calculations

The spin-polarized Kohn-Sham DFT [22, 23] calculations were performed by using the Quantum ESPRESSO software package [24] with the Projector Augmented-Waves (PAW) type pseudopotentials [25]. The exchange-correlation functional was treated in the Perdew-Burke-Ernzerhof (PBE) type of generalized gradient approximation (GGA) [26]. The electronic wavefunction was expressed as a planewave summation truncated at an energy cutoff of 1,360 eV and the electron density was represented on a grid with an energy cutoff of 5500 eV. A periodic 6×6 graphene with lattice parameters  $a = b = 14.76 \text{ \AA}$  and  $\gamma = 120^\circ$  was used as a basis and Fe-N<sub>4</sub> site were embedded in the center of the graphene sheet to construct the Fe-N<sub>4</sub> model (Figure S2). An Fe-N<sub>4</sub> structure in a graphene matrix coupled with pyridinic N was built to model the twin-layer atomic Fe-N<sub>5</sub> structure (Figure S2) [27, 28]. The vacuum spacing was set to 20 Å to avoid the interactions between neighboring sheets. The Brillouin zone integration was performed within the Monkhorst-Pack scheme [29] using the k-points set of 2×2×2. The semiempirical Grimme's DFT-D2 [30] was applied in order to determine the influence of Van der Waals force on the adsorption of intermediates on active site. All atoms were allowed to relax until the calculated forces were converged to better than 5 meV/Å. The charge density difference was evaluated using the formula  $\Delta\rho = \rho(A+B) - \rho_A - \rho_B$ , where  $\rho_X$  is the electron charge density of X.

## Preparation and culture of 3D cancer cells model

Human lung adenocarcinoma cells (A549) were cultured in DMEM, 10% FBS, and 100x Penicillin-Streptomycin-Amphotericin B. They grew in carbon dioxide incubator at with 5% CO<sub>2</sub> and 95% atmospheric humidity at 37°C. For establishing 3D cancer cell model, cells were seeded into Matrigel (Corning, USA) with Y27632 (Selleck, USA) on the first day. Change medium every other day. After 7 days, the single cell grew into 3D cancer cell colony. Then the Matrigel was degraded using Dispase II protease at 37°C. And colonys were collected and used 0.25% trypsin (w/v) containing 0.52 mM EDTA to digested into the single cell to conduct the following experiments.

## Cell viability assay by Cell Counting Kit-8 (CCK-8)

A549 were seeded into 96-well plate to grow into 3D cancer cell colony. Fe-N<sub>5</sub>/GN SAC were diluted into cell medium. Different concentrations of Fe-N<sub>5</sub>/GN SAC including 1, 5, 10, and 20 µg/mL treated 3D cancer cell colony for 24, 48, and 72 h. Then the medium contained Fe-N<sub>5</sub>/GN SAC were discarded. 100 µL new medium were added into each well. 10 µL CCK-8 (Beyotime, China) were added into each well to incubate with cells at the same time. After incubation for 1 h, the absorbance at 450 nm of each well in 96-well plate was detected using microplate reader.

## Cell cytotoxicity assay by LDH Assay Kit

For detect the cell cytotoxicity of Fe-N<sub>5</sub>/GN SAC, we used LDH assay Kit (Beyotime, China). This kit would detect the activity of lactate dehydrogenase (LDH) released into the cell medium to achieve the

determination of cytotoxicity. This parameter could indicate the cell membrane integrity. First, A549 cells were seeded into the 96-well plate for 7 days to grow into the 3D cancer cell colony. Then, used PBS wash cells once and prepared to added Fe-N<sub>5</sub>/GN SAC and other reagents. The wells were divided into different groups: blank control group(only cell medium), control group (only cell), positive group (maximum enzyme activity), and sample group (20 and 50 µg/mL Fe-N<sub>5</sub>/GN SAC). All cells were cultured for 24 h. And the cell culture medium in each well were collected and detected by the kit. The cell cytotoxicity could be calculated as this formula:

$$\text{cell cytotoxicity (\%)} = \frac{OD_{\text{sample}} - OD_{\text{control}}}{OD_{\text{maximum}} - OD_{\text{control}}} \times 100\%$$

### **Cellular ROS level by ROS Assay Kit**

Cellular ROS level was measured using ROS assay Kit (Beyotime, China). DCFH-DA is one type of fluorescence probe and could free access to cell membrane. When it enters into cells, cellular esterase could hydrolyze it to DCFH. And DCFH can't pass through the cell membrane and loaded into cells. Then cellular ROS could oxidize non-fluorescent DCFH to achieve fluorescent DCF. So we can detect the cellular ROS level. A549 cells were seeded into 12-well plate for 7 days to grow to 3D cancer cell colony. Cells were treated and divided into different groups, including control group (only cells), positive group (200 µM H<sub>2</sub>O<sub>2</sub> treatment for 4 h), and sample group (20 µg/mL Fe-N<sub>5</sub>/GN SAC treatment for 24 h). In each group, there were three repeat wells. Then, cells were digested with Dispase II and trypsin protease continuously. Finally, single cells were collected and analyzed using flow cytometry.

### **Cell apoptosis by Annexin V-FITC Apoptosis Detection Kit**

Cell apoptosis was measured using Annexin V-FITC Apoptosis Detection Kit (Beyotime, China). In this kit, Annexin V could selectively bind with phosphatidylserine (PS) distributing into the inside the cell. At the initial stage of cell apoptosis, PS could be exposed to bind with Annexin V-FITC. For late apoptotic cells, the integrity of destroy cell membrane would be destroyed. Propidium Iodide (PI) is one type of nucleic acid dyes and couldn't transfer the whole cell membrane and enter into cell. However, when cell apoptosis occurs, PI enters into cells and dyes cell nucleus. Based on these, we can detect cell apoptosis using this kit. In the assay, we seeded A549 cells in the 12-well plate for 7 days to grow to 3D cancer cell colony. Cells were treated and divided into different groups, including control group (only cells) and sample group (20 and 50 µg/mL Fe-N<sub>5</sub>/GN SAC treatment for 24 h). Three repeat wells in each group were conducted. Also cell colony were digested into single cells. Then, cells were collected and dyed with the kit to perform the flow cytometry analysis.

### **Expression levels of apoptotic-related genes by RT-PCR assay**

Cells were seeded into 12-well plate for 7 days to grow to 3D cancer cell colony. Then they were treated with 20 µg/mL Fe-N<sub>5</sub>/GN SAC for 24 h. Cell colony were digested into single cells. And single cells were

collected into TRIzol reagent (CW BIO, China) for 10 min on the ice. Then add chloroform and centrifuge at 12,000 rpm for 10 min at 4°C. Collect the upper layer into a new RNA-free tube and add isopropanol for 15 min on the ice. Then centrifuge at 12,000 rpm for 20 min at 4°C again. Discard the supernate and use 75% ice ethanol to wash the sediment and centrifuge at 12,000 rpm for 10 min at 4°C. Finally, we discard the supernate and collect RNA.

After that, reverse transcription-polymerase chain reaction (RT-PCR) was conducted. First, reverse transcription was performed with the FastQuant RT kit (Tiangen, China). We can achieve the cDNA. Second, cDNA, primers, RealMasterMix (Tiangen, China), and ddH<sub>2</sub>O were mixed to conduct the RT-PCR using a 7500 Real-Time PCR System (Applied Biosystems, USA). The system was set as 95°C for 5 min, 40 cycles of 95°C for 30 s, 65°C for 30 s, and 72°C for 30 s [31]. The relative expression of genes was calculated as  $2^{-\Delta\Delta C_t}$ . The primers showed in **Table S4**.

## Results

### Synthesis of Fe-N<sub>5</sub>/GN SAC

The synthetic process of Fe-N<sub>5</sub>/GN SAC is shown in Scheme 1a-d. Typically, pyrrole monomer was adsorbed and then coated on graphene oxide by chemical oxidative polymerization to achieve the graphene oxide/polypyrrole (GO/PPy). The wet GO/PPy hybrid was then dispersed in the mixture solution of potassium chloride and potassium ferricyanide to obtain Fe/K-modified GO/PPy (GO/PPy-Fe/K) precursor. This hybrid precursor was pyrolyzed at 900°C under N<sub>2</sub> atmosphere for 30 min and NH<sub>3</sub> atmosphere for 30 min. The obtained carbon material was then subjected to acidic leaching and secondary heat-treatment to achieve Fe-N<sub>5</sub>/GN SAC. Then, the catalytic activity of Fe-N<sub>5</sub>/GN SAC was detected in vitro, such as the peroxidase-like catalytic activity. Next, we used a 3D cancer cell model for exploring the effects of Fe-N<sub>5</sub>/GN SAC in lung cancer therapy (Scheme 1e). Human lung adenocarcinoma cell (A549) were seeded into Matrigel for 7 days to establish the 3D cancer cell model. Results showed that 20 µg/mL Fe-N<sub>5</sub>/GN SAC could decrease cell viability to 50% at 24 h. The concentration and the time were chosen as the following experimental treatment conditions. Furthermore, we detected the production of ROS and cell apoptosis induced by the novel Fe-N<sub>5</sub>/GN SAC under mild acidity microenvironment of 3D cancer cell model. Also, we preliminarily explored apoptotic-related signaling pathway to reveal the molecular mechanism, which is involved in lung cancer therapy.

### Characterization of Fe-N<sub>5</sub>/GN SAC

The morphology and structure of Fe-N<sub>5</sub>/GN SAC were characterized by SEM and TEM. As shown in Fig. 1a and 1b, Fe-N<sub>5</sub>/GN SAC inherits the structure of graphene oxide, showing nanosheet structure. The size of nanosheets is a few hundred nanometers. High-resolution TEM image in Fig. 1c shows that the nanosheet plane is enriched with abundant distorted well-graphitized carbon layers. Such structure endows Fe-N<sub>5</sub>/GN SAC with abundant defects and defective N doping species (pyridinic N and/or pyrrolic N). Furthermore, no nanosized metal species were detected, suggesting that Fe in Fe-N<sub>5</sub>/GN SAC can be

in the form of isolated atoms and/or nanoclusters. To further verify the Fe species in Fe-N<sub>5</sub>/GN SAC, X-ray absorption fine structure measurements were performed. Figure 1d shows Fourier-transform X-ray absorption fine structure (EXAFS) curve of Fe-N<sub>5</sub>/GN SAC. The scattering peak at 1.4 Å is attributed to Fe-N species while the Fe-Fe scattering peak at 2.1 Å and any other long-range-order scattering peaks are not detected, which demonstrates that Fe is atomically dispersed in Fe-N<sub>5</sub>/GN SAC. Furthermore, to achieve the quantitative structural parameters of single Fe atoms in Fe-N<sub>5</sub>/GN SAC, EXAFS fitting was carried out (Fig. 1e). According to fitting parameters (Table S1), the coordination number of Fe-N in Fe-N<sub>5</sub>/GN SAC is about 5. Figure 1f shows X-ray absorption near-edge structure (XANES) curve of Fe-N<sub>5</sub>/GN SAC. The position of the absorption edge is between those of standard FeO and Fe<sub>2</sub>O<sub>3</sub>, suggesting that the oxidation state of Fe in Fe-N<sub>5</sub>/GN SAC is between 2+ and 3+.

To directly observe the Fe species, we performed high-angle annular dark-field scanning TEM (HAADF-STEM) imaging. As shown in Fig. 2a, large numbers of isolated Fe atoms in Fe-N<sub>5</sub>/GN SAC are observed, which is revealed by the bright dots marked by red cycles. Auxiliary energy-dispersive X-ray spectroscopy (EDS) elemental analysis was performed to detect the chemical composition. As shown in Fig. 2b, C, N, O, and Fe were detected in Fe-N<sub>5</sub>/GN SAC, suggesting that nitrogen coordinated with Fe atoms can be incorporated into the carbon matrix. Illustratively, the Si signal is attributed to the EDS probes while Cu signal originates from the TEM grid. To further reveal the composition of Fe-N<sub>5</sub>/GN SAC, X-ray photoelectron spectroscopy (XPS) was carried out. Figure 2c shows that the N and Fe contents are 6.02 at.% and 0.36 at.%, respectively, in well agreement with previous reports about single-atom Fe-N-C materials [32–34]. On the basis of binding energies, the high-resolution N 1s spectrum was fitted with four peaks at 398.4, 400.1, 401.0, and 402.7 eV (Fig. 2d) [35, 36]. The first one is attributed to pyridinic N or Fe-N<sub>x</sub> because of their similar binding energies [37, 38]. The Fe-N<sub>5</sub>/GN SAC holds high pyridinic N (Fe-N<sub>x</sub>) ratio of 58.6% and is expected to use as high-activity nano-catalyst.

## Evaluation of enzyme-like properties of Fe-N<sub>5</sub>/GN SAC

Given the structural similarity between heme cofactor of peroxidase and atomic Fe-N<sub>5</sub> decorated graphene nanosheet (Supporting information, Figure S1), we investigated the intrinsic peroxidase-like catalytic activity of the as-prepared atomic Fe-N<sub>5</sub>/GN SAC by colorimetric assays. We used the oxidation of 3,3',5,5'-tetramethylbenzidine (TMB) as a model catalytic reaction to investigate the interaction of H<sub>2</sub>O<sub>2</sub> molecules with atomic Fe-N<sub>5</sub> decorated graphene nanosheet. According to the standardized protocol, the typical reactions of TMB colorimetric catalyzed by atomic Fe-N<sub>5</sub> decorated graphene nanosheet were conducted within 1200 s and typical iamges for color change from colorless to characteristic blue were obtained (Fig. 3a). Additionally, an initial resction period of 60 s was observed based on linear-regression analysis ( $R^2 = 0.9997$ ) (Fig. 3b). These results indicated that the as-prepared atomic Fe-N<sub>5</sub> decorated graphene nanosheet possesses excellent enzyme-like characteristics and can be applied as a good SAC candidate.

We further evaluated the potential effects of various harsh environments on the peroxidase-like activity of Fe-N<sub>5</sub>/GN SAC. Over a pH range of 2.5–9.5, no obvious reactions were observed on Fe-N<sub>5</sub>/GN SAC when the pH was greater than 4.5 (Fig. 3c), which suggested that the reaction preferred acidic conditions with an optimal pH value of 3.5. We then evaluated how temperature affects the Fe-N<sub>5</sub>/GN SAC performance. A temperature screen showed that Fe-N<sub>5</sub>/GN SAC maintained above 60% activity from 4 to 70°C and exhibited the highest catalytic activity at 37°C (Fig. 3d). Considering that Fe-N<sub>5</sub>/GN SAC would be used in kinging A549 cells, 37°C was selected as the standard temperature for the subsequent activity analysis and biosensing application.

Under optimal conditions, the catalytic activity units (U) of Fe-N<sub>5</sub>/SAC plotted against their masses were obtained (Fig. 3e). After yielding a unity slope, the specific activity (SA) of the Fe-N<sub>5</sub>/SAC as a peroxidase mimic was determined to be 71.999 U/mg, which is higher than reported Fe-N<sub>x</sub>/SAC and conventional nano-catalysts (Supporting information, Table S2). The evaluation of catalytic kinetics of Fe-N<sub>5</sub>/SAC were obtained by fitting the curves with the Michaelis-Menten equation (Fig. 3f). The steady-state kinetics parameter of Fe-N<sub>5</sub>/SAC in terms of catalytic rate constant ( $K_m$ ) showed its superior binding affinity of TMB compared to natural HRP (Supporting information, Table S3).

## Generation of hydroxyl radicals by Fe-N<sub>5</sub>/GN SAC catalysis

Previous reports have demonstrated that the superior peroxidase-like activity of SACs is attributed to their high capacity of catalyzing H<sub>2</sub>O<sub>2</sub> to generate hydroxyl radicals ( $\cdot\text{OH}$ ) [15, 39, 40]. To elucidate the origin of the excellent peroxidase-like activity of Fe-N<sub>5</sub>/GN SAC, we performed density functional theory (DFT) calculations to investigate the reaction process of generation of hydroxyl radicals through catalyzing H<sub>2</sub>O<sub>2</sub>. The proposed reaction process [15, 39] for generating hydroxyl radical under acidic catalytic milieu for Fe-N<sub>5</sub> model is shown in Fig. 4a. The H<sub>2</sub>O<sub>2</sub> molecule is firstly adsorbed on Fe active site in the Fe-N<sub>5</sub> (Fig. 4a(ii)). The activated H<sub>2</sub>O<sub>2</sub><sup>\*</sup> molecules easily dissociate and then a hydroxyl group desorbs from the adsorbed site, leading to the generation of an active hydroxyl radical and a hydroxyl group adsorbed at the single Fe site (Fig. 4a(iii)). The adsorbed hydroxyl group reacts with protonated hydrogen atom under acidic conditions, forming an H<sub>2</sub>O<sup>\*</sup> molecule adsorbed on Fe active site. The catalyst surface returns to its free state (Fig. 4a(i)) after the desorption of this adsorbed H<sub>2</sub>O<sup>\*</sup> molecule [41, 42]. Differently, the adsorbed H<sub>2</sub>O<sub>2</sub><sup>\*</sup> on Fe active site in the Fe-N<sub>4</sub> model is spontaneously cleaved homolytically into two OH<sup>\*</sup> species adsorbed on Fe atom (Figure S3) [6, 43]. One of the adsorbed OH<sup>\*</sup> subsequently dissociates and desorbs from adsorbed site and forms an active intermediate  $\cdot\text{OH}$ , leaving a OH<sup>\*</sup> adsorbed on Fe atom. According to the free energy diagram shown in Fig. 4b, the adsorption of H<sub>2</sub>O<sub>2</sub> on Fe active site is downhill in free energy, indicating the thermodynamical favor of this step for both Fe-N<sub>5</sub> and Fe-N<sub>4</sub> models. Moreover, the adsorption of H<sub>2</sub>O<sub>2</sub> on Fe active site in Fe-N<sub>4</sub> model is stronger than that in Fe-N<sub>5</sub> model, leading to the homolytic cleavage of adsorbed H<sub>2</sub>O<sub>2</sub><sup>\*</sup> into two OH<sup>\*</sup> species (Figure S3). The rate determining step (RDS) is the generation of a reactive hydroxyl radical and an adsorbed hydroxyl group for both Fe-N<sub>5</sub> and Fe-N<sub>4</sub> models with the energy barrier of 0.72 eV and 1.23 eV, respectively (Fig. 4b),

indicating that the single Fe active site in Fe-N<sub>5</sub> model is energetically more favorable for the reaction process of generation of hydroxyl radical. This results in a higher peroxidase-like activity for Fe-N<sub>5</sub> model, which is in good agreement with our experimental observations.

Figure S4 shows the projected density states (PDOS) of  $d$ ,  $d_{z^2}$  and  $d_{x^2-y^2}$  orbitals of Fe atom in Fe-N<sub>5</sub> and Fe-N<sub>4</sub> models. The PDOS curves of  $d$ ,  $d_{z^2}$  and  $d_{x^2-y^2}$  orbitals of Fe atom in Fe-N<sub>5</sub> model are significantly different compared with that in Fe-N<sub>4</sub> model due to the charge transfer from pyridinic N layer to Fe atom, as shown in Fig. 4c, indicating that the number of electrons filled in these orbitals are different between Fe atoms in these two models. Integration of PDOS of an orbital to the Fermi level obtains the number of electrons filled in that orbital. There are more electrons filled in  $e_g$  orbitals ( $d_{z^2}$  and  $d_{x^2-y^2}$ ) of the Fe atom in the Fe-N<sub>5</sub> model than that in the Fe-N<sub>4</sub> model (Fig. 4d), implying the weaker binding strength between the Fe atom and the H<sub>2</sub>O<sub>2</sub>\* for the Fe-N<sub>5</sub> model. This can be confirmed by the  $d$ -band center analysis. The  $d$ -band center of Fe atom in the Fe-N<sub>5</sub> model (-1.13 eV) is further with the respect to the Fermi level than that in the Fe-N<sub>4</sub> model (-0.98 eV), indicating the weaker bonding interaction between the Fe atom and the intermediates for the Fe-N<sub>5</sub> model, thus contributing to the superior catalytic performance.

## Cell killing effects of Fe-N<sub>5</sub>/GN SAC

To investigate whether the excellent Fe-N<sub>5</sub>/GN SAC is compatible with biomedical application, we explored the potential of Fe-N<sub>5</sub>/GN SAC in cancer therapy. Firstly, we established the 3D cancer cell model by seeding A549 cells into Matrigel. After 7 days, the single cell embedding in the matrix proliferated into the colony of tumor cell to form the 3D cancer cell model (Fig. 5a). For evaluating the cytotoxicity of Fe-N<sub>5</sub>/GN SAC, it incubated with the 3D model for 24, 48 and 72 h at different concentrations. Results showed us that concentration-dependent cytotoxicity could be observed and the cell viabilities decreased to about 55%, 70%, and 77%, respectively, at a concentration of 20  $\mu$ g/mL Fe-N<sub>5</sub>/GN SAC (Fig. 5b). The cell killing efficiency of Fe-N<sub>5</sub>/GN SAC was the highest at 24 h. The killing efficiencies of Fe-N<sub>5</sub>/GN SAC were almost same at same concentrations at 48 and 72 h. The result might be that Fe-N<sub>5</sub>/GN SAC entering into the colony and taken up by cells is used up by intracellular H<sub>2</sub>O<sub>2</sub>, while, there is still some cells alive. If the addition of Fe-N<sub>5</sub>/GN SAC is not continuous, the alive cells will play a leading role in the colony. And the cell viability would have a bounced back. Therefore, the cell viabilities at 48 and 72 h are higher than that at same concentrations at 24 h. Here, we also detected the cell viability in control group. There is no any significant changes (Data not shown). Based on these results, we chose 20  $\mu$ g/mL and 24 h as the concentration and timepoint of Fe-N<sub>5</sub>/GN SAC treatment. In addition, we also detected the LDH release level after Fe-N<sub>5</sub>/GN SAC treatment. Comparing with that in control group, we found that 20 and 50  $\mu$ g/mL Fe-N<sub>5</sub>/GN SAC enhanced significantly the LDH release in 3D cancer cell model (Fig. 5c). However, they are a little decrease than that in positive group. It proved that the addition of Fe-N<sub>5</sub>/GN SAC resulted in the membranolysis, which could induce the LDH release into the cell culture medium.

The hypoxic condition in tumor has been known, and it could promote the invasiveness and metastasis, angiogenesis, suppressing immune reactivity, increasing the generation of ROS and antioxidant capacity [44]. Here, we examined the ROS level after Fe-N<sub>5</sub>/GN SAC incubation. The result showed us that Fe-N<sub>5</sub>/GN SAC could increase significantly the ROS level. And the increase is higher than that in positive group (H<sub>2</sub>O<sub>2</sub> incubation) (Fig. 5d and 5e). It could be predicted that the oxidative stress happened in 3D cancer cell model. Moreover, the cell apoptosis after 20 and 50 µg/mL Fe-N<sub>5</sub>/GN SAC incubation was investigated. We knowed that this SAC induced cell apoptosis to some extent. The percents of cell apoptosis were about 10% and 15%, respectively (Fig. 6a and 6b). There are significant increases than that in control group. However, the changes were not as much as that in ROS levels.

Finally, we tried to explore the changes of the expression levels of apoptotic-related genes, including *Caspases-3*, *Caspase-9*, *Bcl-2*, and *Bax*. Results showed us that the expression levels of *Cas-3*, *Cas-9*, and *Bcl-2* increased significantly after 20 µg/mL Fe-N<sub>5</sub>/GN SAC incubation for 24 h (Fig. 6c). While, no change in the expression level of *Bax* (Fig. 6c). It has been reported that ROS also can induce mitochondria damage, which further activated *Cas-9*. Next, caspase cascade was triggered. That is to say, *Cas-3*, *6*, *7* activated to induce further cytotoxicity [45, 46]. Finally, cell apoptosis happened. *Bcl-2* is the oncogene, and could inhibit ROS-induced cell apoptosis [47]. Its increase might be the resistance response of tumor cells after Fe-N<sub>5</sub>/GN SAC incubation. However, for revealing the molecular mechanism, much more explorations need to be done. All these changes indicated that Fe-N<sub>5</sub>/GN SAC is of promising cancer therapy.

## Discussion

### Exploration of the stronger adsorption of H<sub>2</sub>O<sub>2</sub> on Fe active site

In this study, the filling degree of atomic d orbital of active metal plays a crucial role in the binding strength of adsorbate to the active metal atom [48]. Specifically, e<sub>g</sub>-like orbitals (*d*<sub>z<sup>2</sup></sub> and *d*<sub>x<sup>2</sup>-y<sup>2</sup></sub>) of the active metal atom significantly effect on the bonding interaction between adsorbate and active site because of their favorable vertical orientation toward intermediates [48]. With the increase of number of electrons filled in e<sub>g</sub> orbital of active metal atom, the binding interaction between intermediates and active metal site decreases due to the increased filling degree of antibonding states [49]. Here, the electronic structures of Fe atom were calculated to obtain the number of electrons filled in Fe *d* orbital in Fe-N<sub>5</sub> and Fe-N<sub>4</sub> models, therefore explaining the stronger adsorption of H<sub>2</sub>O<sub>2</sub> on Fe active site in Fe-N<sub>4</sub> model.

### Exploration of killing effects of Fe-N<sub>5</sub>/GN SAC

In this study, 3D cancer cell model was chosen as the *in vitro* model for exploring the killing effects of Fe-N<sub>5</sub>/GN SAC. The model is more precise to show the realistic response, which closed to the natural

conditions *in vivo*. 3D culture system is used widely in drug screen, cell biology, and developmental biology. Moreover, 3D model could maintain cell-to-cell and cell-to-matrix interaction, which is important to explore all life processes *in vivo* [20]. Therefore, we used the 3D cancer cell model to exploration the killing effects of Fe-N<sub>5</sub>/GN SAC.

In addition, The excellent killing effects were induced by enzyme-like properties of Fe-N<sub>5</sub>/GN SAC. In general, tumor cells have an accelerated metabolism and demand high ROS concentrations to maintain their high proliferation rate [50]. Thus, there are two therapies targeting the oxidative stress in tumor cells, antioxidant and pro-oxidant therapy. Antioxidants could scavenge overproducing ROS and decrease the metabolism of tumor cell to inhibit the proliferation [51]. Applications of pro-oxidant somehow seems contradictory with the upper therapy. However, it could be understood as “Hair of the dog that bit you”. Same with classical cancer drug, 5-fluorouracil (5-FU) and oxaliplatin, it could induce increase the ROS level *in vitro* and *in vivo*. Both of them have been used in cancer therapy. It could also be speculated that the capacity of anti-oxidative stress was enhanced in tumor cells. While, the overproducing ROS might exceed the capacity and induce antioxidative system collapse to dysfunction of cells. Furthermore, it has been reported that oxidative stress could induce cell apoptosis in multiple cell types, including HepG2 cells [52], breast cancer MDA-MB-231 cells [53], smooth muscle cells [52], et al. The molecular mechanism is that ROS activates several transcription factors, including nuclear factor-Kappa B (NF-κB), p53, and Nrf2, which participate in the activation of apoptosis pathway. After NF-κB activation, it would enter into the cell nucleus and combine with apoptotic-related genes, such as c-myc, to promote the gene transcription and cell apoptosis. Also, ROS could induce DNA break to lead to the activation of polypADP nucleic transferase and accumulation of p53, which could induce the expressions of pro-apoptotic genes [54]. In a word, all of these results proved that the potential of Fe-N<sub>5</sub>/GN SAC to cancer therapy.

## Conclusion

In this study, we presented an example of atomically dispersed Fe-N<sub>5</sub> active sites in graphene nanosheets as SAC and demonstrated its performance for cancer therapy. The new SAC is of unique properties including maximum specific activity, atomic utilization, and especially five-nitrogen-coordinated single-atom Fe sites. Moreover, combining with the characteristics of TME, the excellent peroxidase-like catalytic activity of Fe-N<sub>5</sub>/GN SAC could induce the overproduction of ROS in tumor cells. Furthermore, oxidative stress triggered the occurrence of cell apoptosis, which lead to the tumor cell killing. We believe that this novel SAC has a great potential for cancer therapy.

## Abbreviations

SAC

Single-atom catalyst

Fe-N<sub>5</sub>/GN

Fe-N decorated graphene nanosheet

DFT  
Density functional theory  
H<sub>2</sub>O<sub>2</sub>  
hydrogen peroxide  
TME  
tumor microenvironment  
APS  
ammonium peroxydisulfate  
SEM  
scanning electron microscopy  
PAW  
Projector Augmented-Waves  
PBE  
Perdew-Burke-Ernzerhof  
LDH  
lactate dehydrogenase  
PS  
phosphatidylserine  
PI  
Propidium Iodide  
GO/Ppy  
graphene oxide/polypyrrole  
GO/PPy-Fe/K  
Fe/K-modified GO/PPy  
XANES  
X-ray absorption near-edge structure  
EDS  
energy-dispersive X-ray spectroscopy  
XPS  
X-ray photoelectron spectroscopy  
TMB  
3,3',5,5'-tetramethylbenzidine  
RDS  
rate determining step  
PDOS  
projected density states  
Cas-3  
Caspases-3  
Cas-9  
Caspase-9

5-FU  
5-fluorouracil  
NF-Kb  
nuclear factor-Kappa B

## Declarations

Ethics approval and consent to participate

Not applicable

Consent for publication

Not applicable

Availability of data and materials

All data used to support the findings of this study are available from the corresponding author upon request.

Competing interests

The authors declare no conflict of interest.

Funding

Nan Cheng would like to acknowledge the support the 2115 Talent Development Program of China Agricultural University.

Authors' contributions

All authors contributed to the study. Conceptualization and supervision were performed by Nan Cheng, Jincheng Li, Yuehe Lin. The writing-Original draft preparation were prepared by Liye Zhu. Method and data analysis were conducted by Liye Zhu, Hong Zhong, Tao Li. and Scott P. Beckman. Some resources were provided by Hoai Nguyen. The writing-reviewing and editing were conducted by Dan Du, Wentao Xu, Nan Cheng, Jincheng Li, and Yuehe Lin.

Acknowledgements

Thanks for resources of the Advanced Photon Source, a U.S. Department of Energy (DOE) Office of Science User Facility, operated for the DOE Office of Science by Argonne National Laboratory under Contract No. DE-AC02-06CH11357.

Authors' information

Liye Zhu, Wentao Xu, Nan Cheng: Beijing Laboratory for Food Quality and Safety, College of Food Science and Nutritional Engineering, China Agricultural University, Beijing 100083, China; Hong Zhong, Dan Du, Scott P. Beckman, Yuehe Lin: School of Mechanical and Materials Engineering, Washington State University, Pullman, WA 99164, USA; Tao Li: Department of Chemistry and Biochemistry, Northern Illinois University, 1425 W. Lincoln Hwy., DeKalb, IL, 60115, USA & X-ray Science Division, Argonne National Laboratory, 9700 S. Cass Ave, Lemont, IL, 60439; Hoai Nguyen: Material Science Division, Argonne National Laboratory, 9700 S. Cass Ave, Lemont, IL, 60439; Jincheng Li: Faculty of Chemical Engineering, Yunnan Provincial Key Laboratory of Energy Saving in Phosphorus Chemical Engineering and New Phosphorus Materials, Kunming University of Science and Technology, Kunming, 650500, China

## References

1. Thai AA, Solomon BJ, Sequist LV, et al. Lung cancer. *Lancet*. 2021; 398: 535-554.
2. Li S, Shang L, Xu B, et al. A Nanozyme with Photo-Enhanced Dual Enzyme-Like Activities for Deep Pancreatic Cancer Therapy. *Angew Chem Int Ed Engl*. 2019; 58: 12624-12631.
3. Cheng N, Li JC, Liu D, et al. Single-Atom Nanozyme Based on Nanoengineered Fe-N-C Catalyst with Superior Peroxidase-Like Activity for Ultrasensitive Bioassays. *Small*. 2019; 15: e1901485.
4. Jiao L, Xu W, Fau - Wu Y, Wu Y, Fau - Yan H, et al. Single-atom catalysts boost signal amplification for biosensing. *Chem Soc Rev*. 2021; 50(2): 750-765.
5. Wang X, Fan L, Cheng L, et al. Biodegradable Nickel Disulfide Nanozymes with GSH-Depleting Function for High-Efficiency Photothermal-Catalytic Antibacterial Therapy. *iScience*. 2020; 23: 101281.
6. Xu B, Wang H, Wang W, et al. A Single-Atom Nanozyme for Wound Disinfection Applications. *Angew Chem Int Ed Engl*. 2019; 58: 4911-4916.
7. Wang D, Wu H, Phua SZF, et al. Self-assembled single-atom nanozyme for enhanced photodynamic therapy treatment of tumor. *Nat Commun*. 2020; 11: 357.
8. Luo Y, Song Y, Wang M, et al. Bioinspired Peptoid Nanotubes for Targeted Tumor Cell Imaging and Chemo-Photodynamic Therapy. *Small*. 2019; 15: e1902485.
9. Zhou X, You M, Wang F, et al. Multifunctional Graphdiyne-Cerium Oxide Nanozymes Facilitate MicroRNA Delivery and Attenuate Tumor Hypoxia for Highly Efficient Radiotherapy of Esophageal Cancer. *Adv Mater*. 2021; 33: e2100556.
10. Ning S, Zheng Y, Qiao K, et al. Laser-triggered combination therapy by iron sulfide-doxorubicin@functionalized nanozymes for breast cancer therapy.
11. Cai X, Wang M, Mu P, et al. Sequence-Defined Nanotubes Assembled from IR780-Conjugated Peptoids for Chemophototherapy of Malignant Glioma. *Research (Wash D C)*. 2021: 9861384.
12. Shen L, Ye D, Zhao H, et al. Perspectives for Single-Atom Nanozymes: Advanced Synthesis, Functional Mechanisms, and Biomedical Applications. *Anal Chem*. 2021; 93: 1221-1231.

13. Zhao C, Xiong C, Liu X, et al. Unraveling the enzyme-like activity of heterogeneous single atom catalyst. *Chemical communications*. 2019; 55: 2285-2288.
14. Jiao L, Yan H, Wu Y, et al. When Nanozymes Meet Single-Atom Catalysis. *Angew Chem Int Ed Engl*. 2020; 59: 2565-2576.
15. Xu B, Wang H, Wang W, et al. A Single-Atom Nanozyme for Wound Disinfection Applications. *Angewandte Chemie International Edition*. 2019; 58: 4911-4916.
16. Cheng N, Li JC, Liu D, et al. Single-Atom Nanozyme Based on Nanoengineered Fe–N–C Catalyst with Superior Peroxidase-Like Activity for Ultrasensitive Bioassays. *Small*. 2019: 1901485.
17. Niu X, Shi Q, Zhu W, et al. Unprecedented peroxidase-mimicking activity of single-atom nanozyme with atomically dispersed Fe–Nx moieties hosted by MOF derived porous carbon. *Biosensors and Bioelectronics*. 2019; 142: 111495.
18. Fu S, Zhu C, Su D, et al. Porous Carbon-Hosted Atomically Dispersed Iron–Nitrogen Moiety as Enhanced Electrocatalysts for Oxygen Reduction Reaction in a Wide Range of pH. *Small*. 2018; 14: 1703118.
19. Koledova Z 3D Cell Culture: An Introduction. *Methods Mol Biol*. 2017; 1612: 1-11.
20. Ravi M, Paramesh V, Kaviya SR, et al. 3D cell culture systems: advantages and applications. *J Cell Physiol*. 2015; 230: 16-26.
21. Jiang B, Duan D, Gao L, et al. Standardized assays for determining the catalytic activity and kinetics of peroxidase-like nanozymes. *Nat Protoc*. 2018; 13: 1506-1520.
22. Hohenberg P, Kohn W Inhomogeneous Electron Gas. *Physical Review*. 1964; 136: B864-B871.
23. Kohn W, Sham LJ Self-Consistent Equations Including Exchange and Correlation Effects. *Physical Review*. 1965; 140: A1133.
24. Perkinson JC, Swenson JM, DeMasi A, et al. Sawtooth structure formation under nonlinear-regime ion bombardment. *J Phys Condens Matter*. 2018; 30: 294004.
25. Kresse G, Joubert D From ultrasoft pseudopotentials to the projector augmented-wave method. *Physical Review B*. 1999; 59: 1758-1775.
26. Perdew JP, Burke K, Ernzerhof M Generalized Gradient Approximation Made Simple. *Phys Rev Lett*. 1996; 77: 3865-3868.
27. Huang L, Chen J, Gan L, et al. Single-atom nanozymes. *Sci Adv*. 2019; 5: eaav5490.
28. Zhang H, Li J, Xi S, et al. A Graphene-Supported Single-Atom FeN<sub>5</sub> Catalytic Site for Efficient Electrochemical CO<sub>2</sub> Reduction. *Angew Chem Int Ed Engl*. 2019; 58: 14871-14876.
29. Monkhorst HJ, Pack JD Special points for Brillouin-zone integrations. *Physical Review B*. 1976; 13: 5188-5192.
30. Grimme S Semiempirical GGA-type density functional constructed with a long-range dispersion correction. *J Comput Chem*. 2006; 27: 1787-99.
31. Zhu L, Wang H, Yuhan J, et al. Exosomes mediated the delivery of ochratoxin A-induced cytotoxicity in HEK293 cells. *Toxicology*. 2021; 461: 152926.

32. Zhu C, Shi Q, Xu BZ, et al. Hierarchically Porous M–N–C (M = Co and Fe) Single-Atom Electrocatalysts with Robust MN<sub>x</sub> Active Moieties Enable Enhanced ORR Performance. *Adv. Energy Mater.* 2018; 8: 1801956.
33. Li J-C, Yang Z-Q, Tang D-M, et al. N-doped carbon nanotubes containing a high concentration of single iron atoms for efficient oxygen reduction. *NPG Asia Mater.* 2018; 10: e461.
34. Li J-C, Xiao F, Zhong H, et al. Secondary-Atom-Assisted Synthesis of Single Iron Atoms Anchored on N-Doped Carbon Nanowires for Oxygen Reduction Reaction. *ACS Catal.* 2019; 9: 5929-5934.
35. Li J-C, Hou P-X, Zhao S-Y, et al. A 3D bi-functional porous N-doped carbon microtube sponge electrocatalyst for oxygen reduction and oxygen evolution reactions. *Energy Environ. Sci.* 2016; 9: 3079-3084.
36. Li J-C, Meng Y, Zhang L, et al. Dual-Phasic Carbon with Co Single Atoms and Nanoparticles as a Bifunctional Oxygen Electrocatalyst for Rechargeable Zn–Air Batteries. *Adv. Funct. Mater.* 2021; 31: 2103360.
37. Liang H-W, Wei W, Wu Z-S, et al. Mesoporous Metal–Nitrogen-Doped Carbon Electrocatalysts for Highly Efficient Oxygen Reduction Reaction. *J. Am. Chem. Soc.* 2013; 135: 16002-16005.
38. Zhu C, Fu S, Song J, et al. Self-Assembled Fe–N-Doped Carbon Nanotube Aerogels with Single-Atom Catalyst Feature as High-Efficiency Oxygen Reduction Electrocatalysts. *Small.* 2017; 13: 1603407.
39. Huo M, Wang L, Wang Y, et al. Nanocatalytic Tumor Therapy by Single-Atom Catalysts. *ACS Nano.* 2019; 13: 2643-2653.
40. Ahmed Y, Yaakob Z, Akhtar P Degradation and mineralization of methylene blue using a heterogeneous photo-Fenton catalyst under visible and solar light irradiation. *Catalysis Science & Technology.* 2016; 6: 1222-1232.
41. Celardo I, Pedersen JZ, Traversa E, et al. Pharmacological potential of cerium oxide nanoparticles. *Nanoscale.* 2011; 3: 1411-1420.
42. Herget K, Hubach P, Pusch S, et al. Haloperoxidase Mimicry by CeO<sub>2-x</sub> Nanorods Combats Biofouling. *Advanced Materials.* 2017; 29: 1603823.
43. Jiao L, Wu J, Zhong H, et al. Densely Isolated FeN<sub>4</sub> Sites for Peroxidase Mimicking. *ACS Catalysis.* 2020; 10: 6422-6429.
44. Jing X, Yang F, Shao C, et al. Role of hypoxia in cancer therapy by regulating the tumor microenvironment. *Mol Cancer.* 2019; 18: 157.
45. Brentnall M, Rodriguez-Menocal L, De Guevara RL, et al. Caspase-9, caspase-3 and caspase-7 have distinct roles during intrinsic apoptosis. *BMC Cell Biol.* 2013; 14: 32.
46. Linder M, Tschernig T Vasculogenic mimicry: Possible role of effector caspase-3, caspase-6 and caspase-7. *Ann Anat.* 2016; 204: 114-7.
47. Rodriguez-Gonzalez J, Wilkins-Rodriguez AA, Gutierrez-Kobeh L Role of glutathione, ROS, and Bcl-xL in the inhibition of apoptosis of monocyte-derived dendritic cells by *Leishmania mexicana* promastigotes. *Parasitol Res.* 2018; 117: 1225-1235.

48. Hwang J, Rao RR, Giordano L, et al. Perovskites in catalysis and electrocatalysis. *Science*. 2017; 358: 751-756.
49. Xia D, Yang X, Xie L, et al. Direct Growth of Carbon Nanotubes Doped with Single Atomic Fe–N<sub>4</sub> Active Sites and Neighboring Graphitic Nitrogen for Efficient and Stable Oxygen Reduction Electrocatalysis. *Advanced Functional Materials*. 2019; 29.
50. Sosa V, Moline T, Somoza R, et al. Oxidative stress and cancer: an overview. *Ageing Res Rev*. 2013; 12: 376-90.
51. Kovacic P, Jacintho JD Mechanisms of carcinogenesis: focus on oxidative stress and electron transfer. *Curr Med Chem*. 2001; 8: 773-96.
52. Wu Z, Wang H, Fang S, et al. Roles of endoplasmic reticulum stress and autophagy on H<sub>2</sub>O<sub>2</sub> induced oxidative stress injury in HepG2 cells. *Mol Med Rep*. 2018; 18: 4163-4174.
53. Cui L, Bu W, Song J, et al. Apoptosis induction by alantolactone in breast cancer MDA-MB-231 cells through reactive oxygen species-mediated mitochondrion-dependent pathway. *Arch Pharm Res*. 2018; 41: 299-313.
54. Kaminsky VO, Zhivotovsky B Free radicals in cross talk between autophagy and apoptosis. *Antioxid Redox Signal*. 2014; 21: 86-102.

## Scheme

Scheme 1 is available in Supplementary Files section.

## Figures

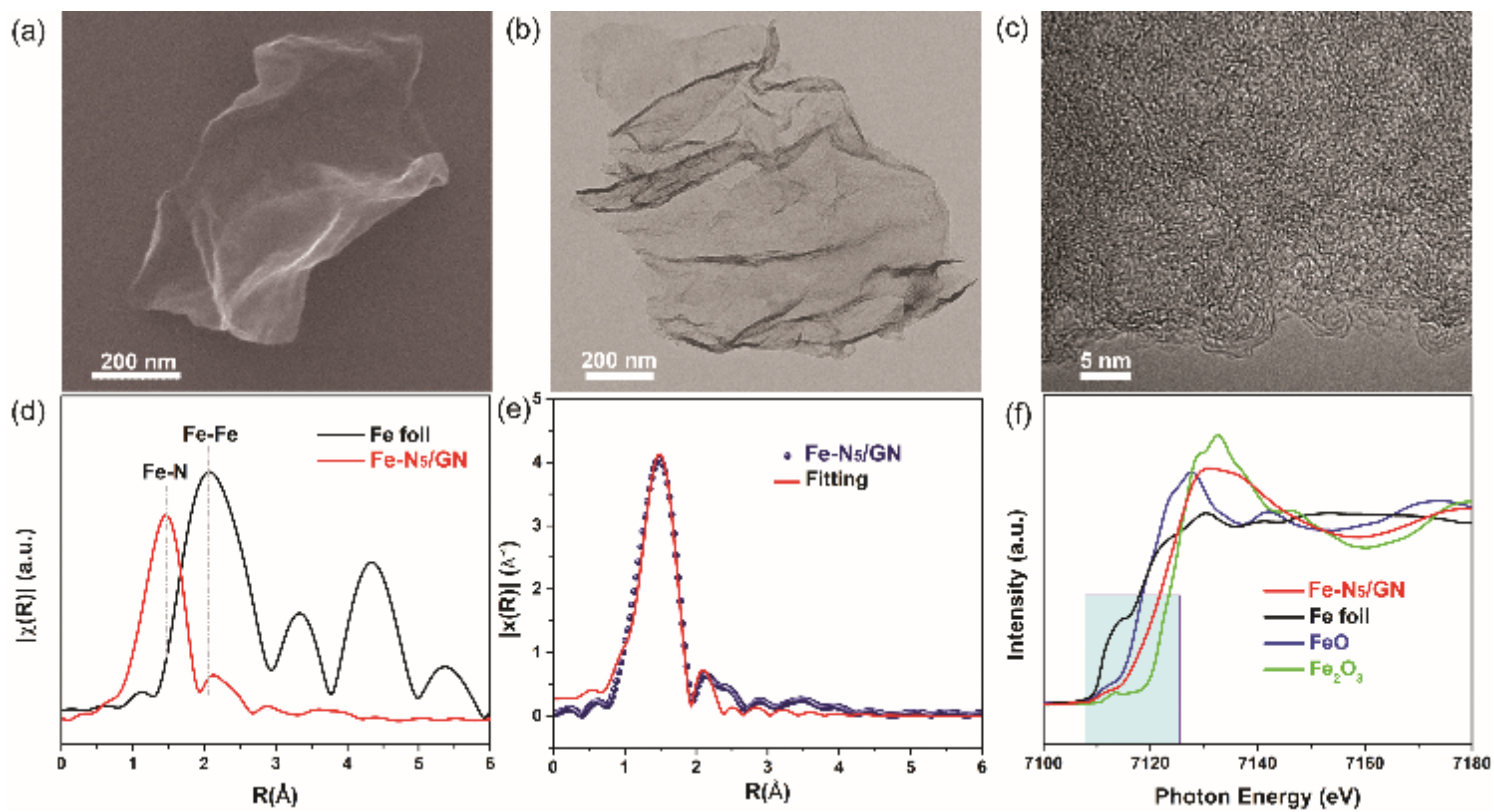


**Figure 1**

(a) SEM and (b) TEM images of Fe-N<sub>5</sub>/GN SAC. (c) Fourier-transform EXAFS, (d) EXAFS fitting, and (f) XANES spectrum of Fe-N<sub>5</sub>/GN SAC and reference samples.

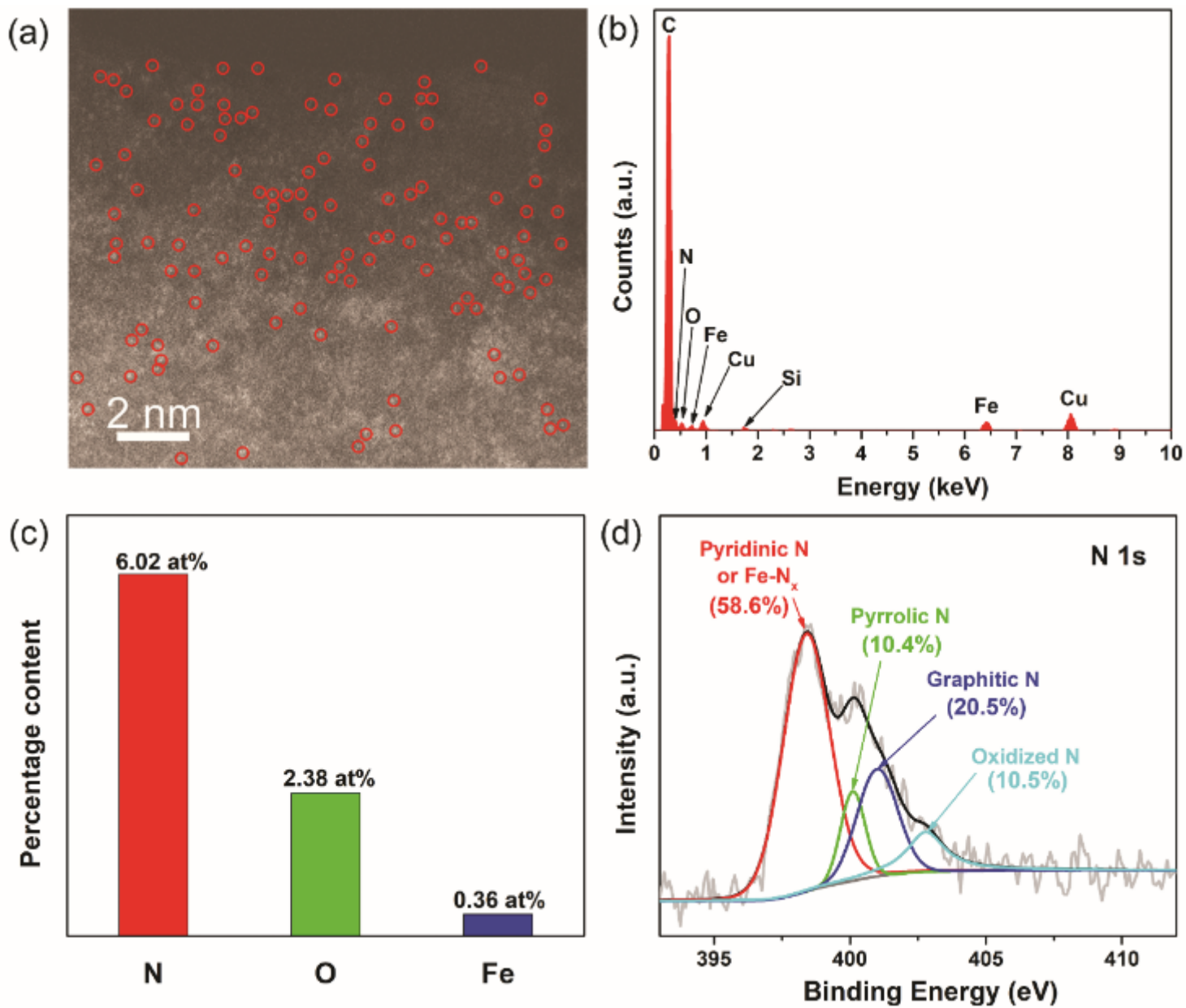
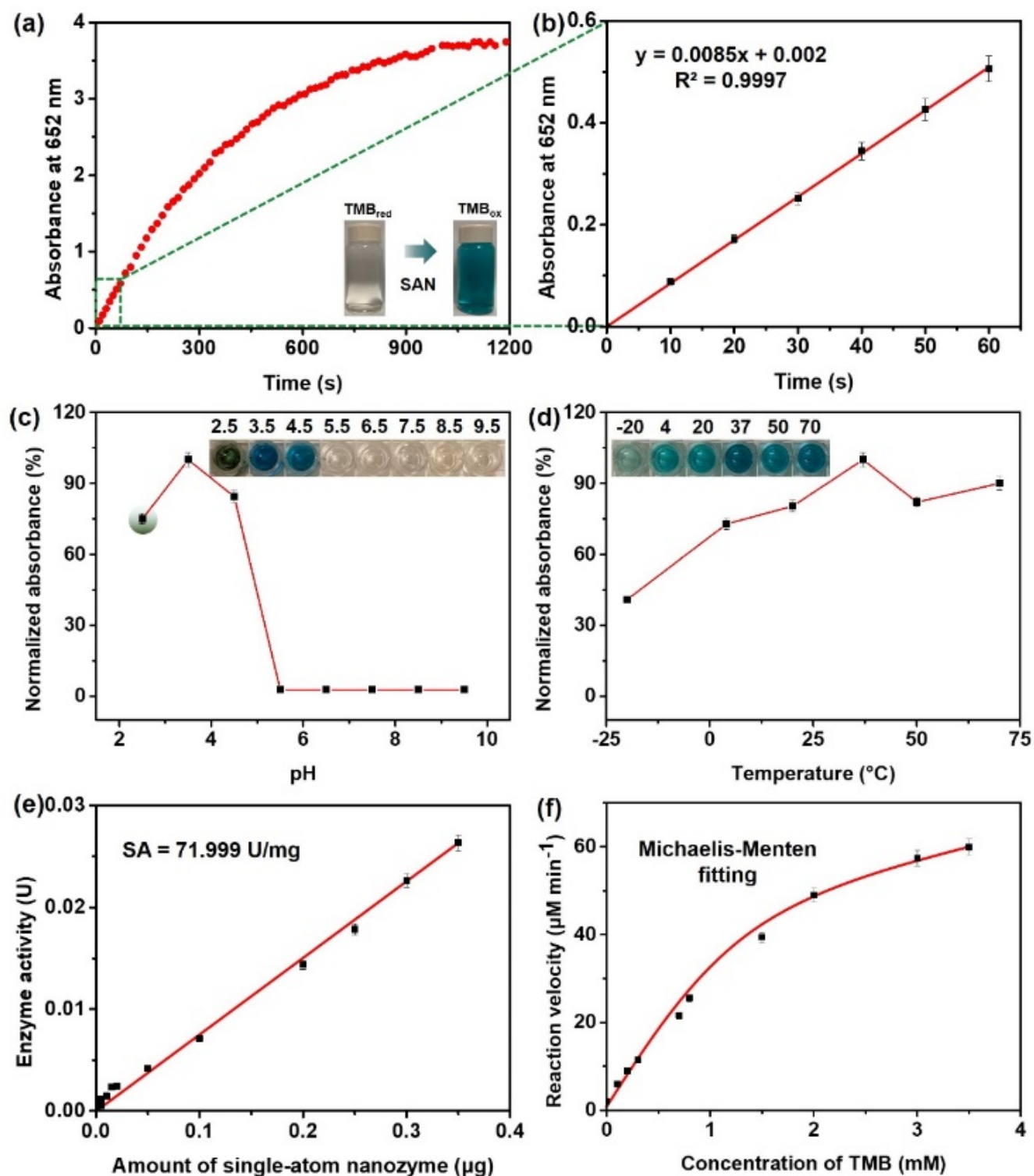


Figure 2

(a) Typical HAADF-STEM and (b) EDS element analysis images of Fe-N<sub>5</sub>/GN SAC. (c) N, O, and Fe contents in Fe-N<sub>5</sub>/GN SAC detected from XPS measurement. (d) N 1s spectra of Fe-N<sub>5</sub>/GN SAC.



**Figure 3**

Intrinsic peroxidase-like catalytic activity of single-atom catalyst. (a) Reaction-time curves of TMB colorimetric reaction catalyzed by single-atom catalyst. (b) The magnified initial linear portion of the single-atom catalyst reaction-time curves. (c) Peroxidase-like catalytic activity of single-atom catalyst against various pH value. (d) Peroxidase-like catalytic activity of single-atom catalyst against various

temperature. (e) The relationship between the enzyme specific activity (SA) of the single-atom catalyst and its amount. (f) Michaelis-Menten fitting curve for Fe-N<sub>5</sub>/SAC toward various concentrations of TMB.

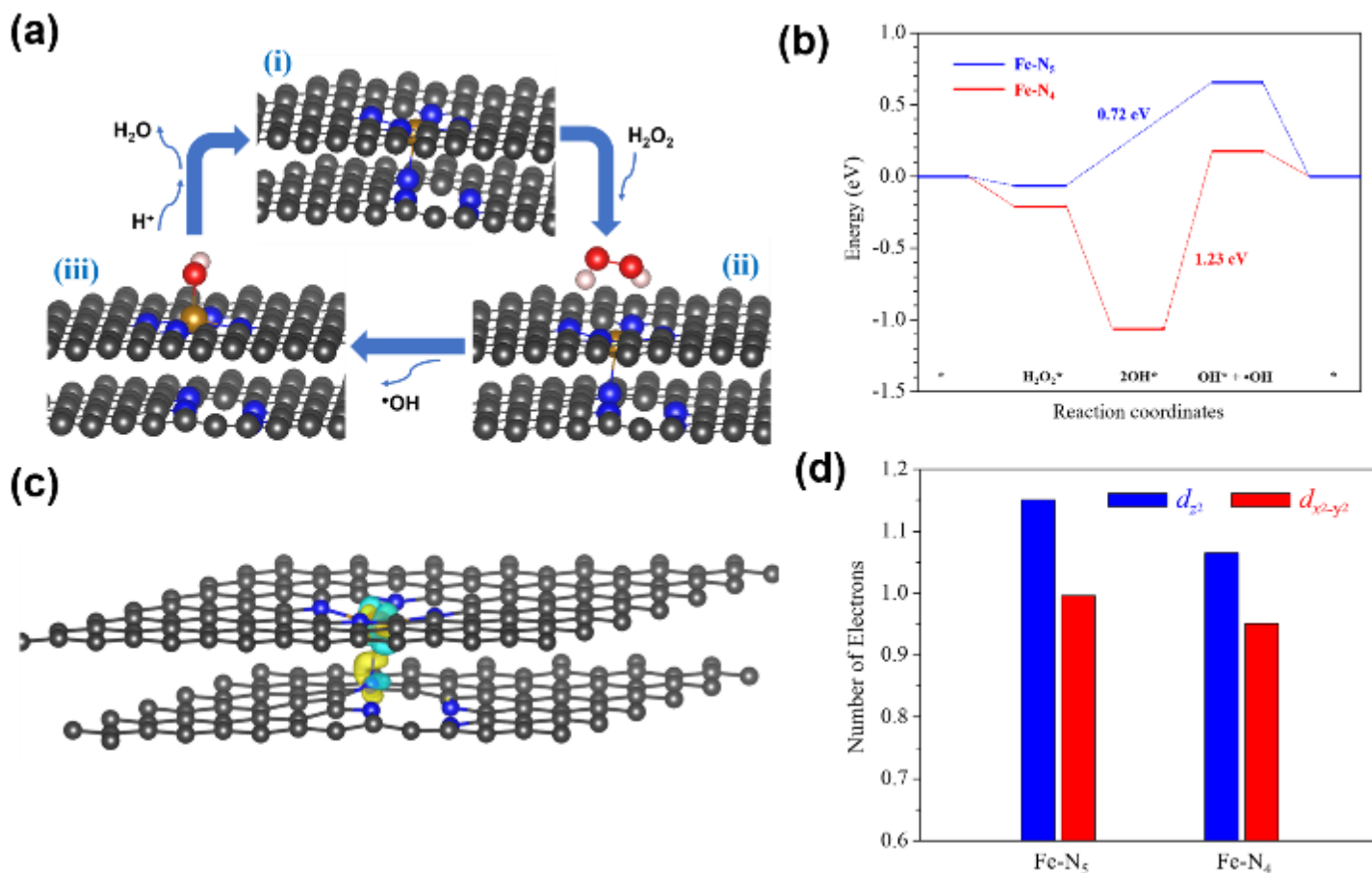


**Figure 4**

(a) Schematic illustration of the proposed reaction process for the Fe-N<sub>5</sub> model under acidic catalytic milieu. The Gray, blue, brown, red, and white balls represent the C, N, Fe, O, and H atoms, respectively. (b) Free energy diagram of the proposed reaction process for the Fe-N<sub>4</sub> and Fe-N<sub>5</sub> models. The \* represents the single Fe active site where the intermediates adsorbed on. (c) Charge density difference which is obtained as the difference between the valence charge density of the twin-layer atomic Fe-N<sub>5</sub> structure and the Fe-N<sub>4</sub> and pyridinic N structure layers. The Gray, blue, and brown balls represent the C, N, and Fe atoms, respectively. Yellow and cyan areas indicate electron accumulation and electron depletion, respectively. The isosurfaces is 0.008 and the color scale is given in units of e/Bohr<sup>3</sup>. (d) Number of electrons filled in  $d_{z^2}$  and  $d_{x^2-y^2}$  orbitals of Fe atom in Fe-N<sub>5</sub> and Fe-N<sub>4</sub> models.

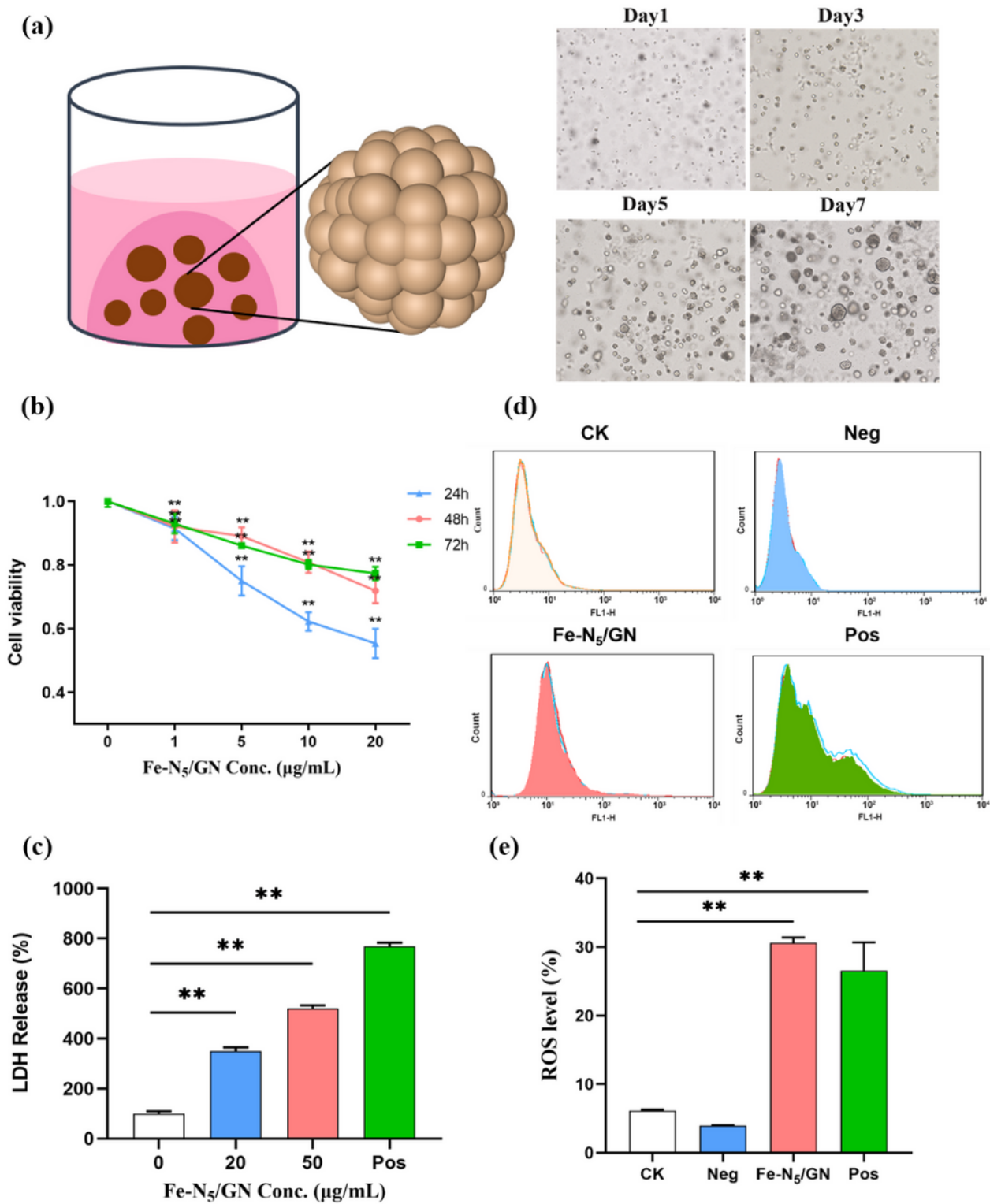


**Figure 5**

(a) Schematic illustration of the 3D cancer cell model. (b) The cell viability after Fe-N<sub>5</sub>/GN SAC incubation at 24, 48, and 72 h. (c) LDH release after Fe-N<sub>5</sub>/GN SAC incubation. (d) ROS level after Fe-N<sub>5</sub>/GN SAC incubation by flow cytometry. (e) Data statistics of ROS level by flow cytometry. \*  $P < 0.05$ , \*\*  $P < 0.01$ .

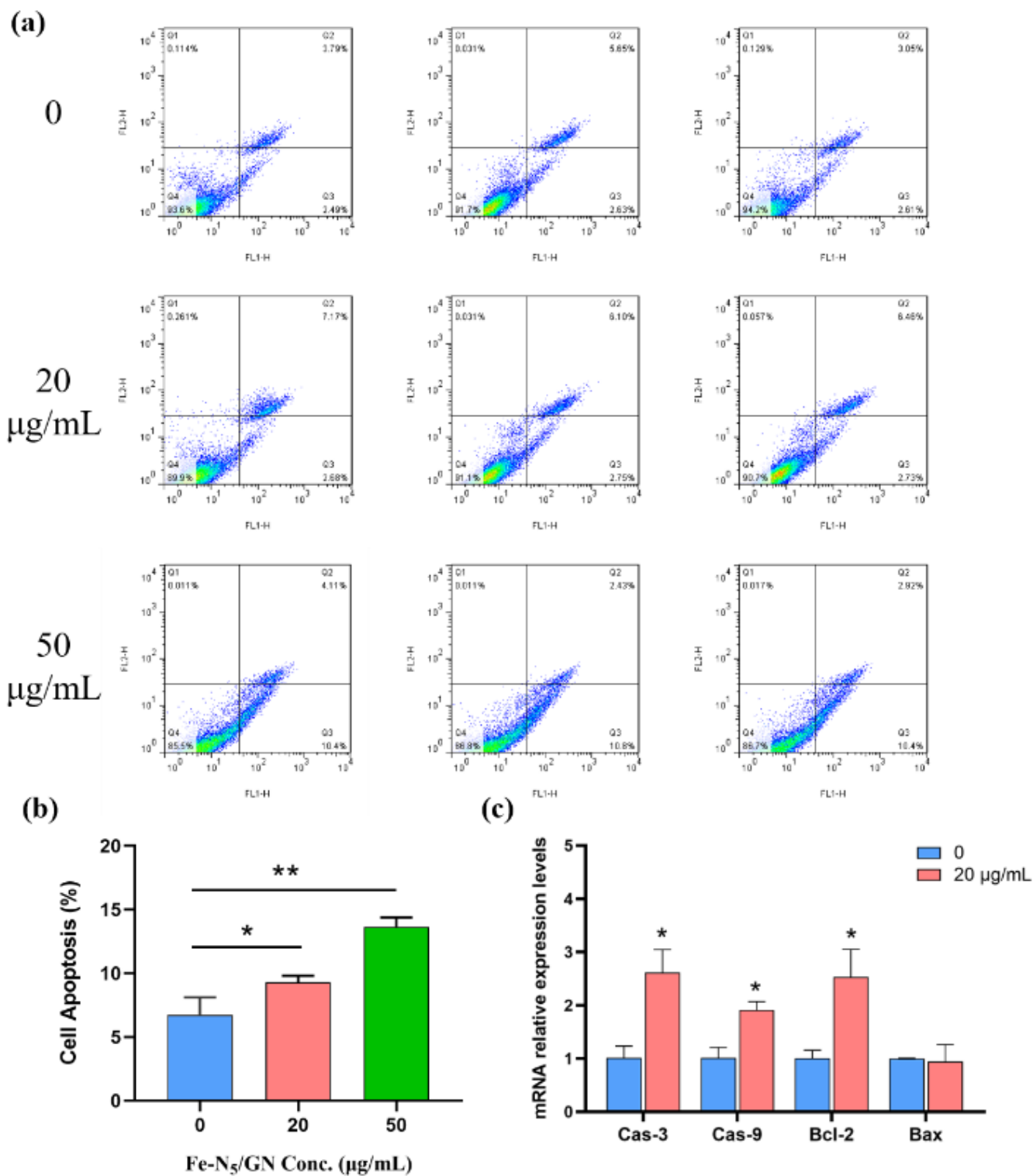


**Figure 6**

(a) Cell apoptosis after Fe-N<sub>5</sub>/GN SAC incubation by flow cytometry. (b) Data statistics of cell apoptosis by flow cytometry. (c) Expression level of apoptotic-related genes, including *Cas-3*, *Cas-9*, *Bcl-2*, and *Bax*. \*  $P < 0.05$ , \*\*  $P < 0.01$ .

## Supplementary Files

This is a list of supplementary files associated with this preprint. Click to download.

- [SupplementInformation.docx](#)
- [Scheme1.png](#)